Discover Oncology

Research

A deep learning model to predict dose distributions for breast cancer radiotherapy

Xiaorong Hou[1] · Weishi Cheng[1,2] · Jing Shen[1] · Hui Guan[1] · Yimeng Zhang[3] · Lu Bai[3] · Shaobin Wang[3] · Zhikai Liu[1]

Received: 3 May 2024 / Accepted: 5 February 2025
Published online: 12 February 2025

Abstract
Purpose In this work, we propose to develop a 3D U-Net-based deep learning model that accurately predicts the dose distribution for breast cancer radiotherapy.
Methods This study included 176 breast cancer patients, divided into training, validating and testing sets. A deep learning model based on the 3D U-Net architecture was developed to predict dose distribution, which employed a double encoder combination attention (DECA) module, a cross stage partial + Resnet + Attention (CRA) module, a difficulty perception and a critical regions loss. The performance and generalization ability of this model were evaluated by the voxel mean absolute error (MAE), several clinically relevant dosimetric indexes and 3D gamma passing rates.
Results Our model accurately predicted the 3D dose distributions with each dosage level mirroring the clinical reality in shape. The generated dose-volume histogram (DVH) matched with the ground truth curve. The total dose error of our model was below 1.16 Gy, complying with clinical usage standards. When compared to other exceptional models, our model optimally predicted eight out of nine regions, and the prediction errors for the first planning target volume (PTV1) and PTV2 were merely 1.03 Gy and 0.74 Gy. Moreover, the mean 3%/3 mm 3D gamma passing rates for PTV1, PTV2, Heart and Lung L achieved 91.8%, 96.4%, 91.5%, and 93.2%, respectively, surpassing the other models and meeting clinical standards.
Conclusions This study developed a new deep learning model based on 3D U-Net that can accurately predict dose distributions for breast cancer radiotherapy, which can improve the quality and planning efficiency.

Keywords Deep learning · Dose prediction · Breast cancer · Dose optimization and planning

1 Introduction

The development of radiotherapy techniques, including intensity-modulated radiation therapy (IMRT), has provided physicians with enhanced flexibility to achieve superior therapeutic effects by delivering high doses to local tumors while minimizing toxicities to normal tissues through dose limitation to adjacent critical structures or organs at risk

Xiaorong Hou and Weishi Cheng contributed to the work equally and should be regarded as co-first authors.

Supplementary Information The online version contains supplementary material available at https://doi.org/10.1007/s12672-025-01942-4.

✉ Zhikai Liu, liuzk2009@126.com | [1]Department of Radiation Oncology, Peking Union Medical College Hospital, Chinese Academy of Medical Sciences and Peking Union Medical College, Beijing 100730, China. [2]Peking Union Medical College, Chinese Academy of Medical Sciences, Beijing 100730, China. [3]MedMind Technology Co. Ltd., AB 1920 Techart Plaza, Beijing 100083, China.

(OARs) [1–3]. However, this approach also increases the complexity of treatment plan design, necessitating repeated adjustments by planners in a trial-and-error manner until the dose distribution meets clinically specific criteria. This process can be time-consuming and heavily reliant on the skills and decisions of individual planners [4–6]. This may lead to significant delays in the formulation and finalization of the plan, as well as subsequent treatments, and considerable variations in the quality of the plan, ultimately resulting in highly negative impacts [6–9]. In breast cancer patients, delaying radiotherapy has been thought to compromise local tumor control and significantly increase the risk of recurrence [10–12]. Special attention is required in planning the irradiation of left-sided breast cancer due to the potential for heart toxicity [13].

The fundamental goal of this process is to generate a high-quality dose distribution. The ability to accurately predict dose distribution can significantly reduce the time required to formulate radiotherapy plans. This enables planners to achieve more precise dose distributions in a shorter period, thereby enhancing the quality and efficiency of radiotherapy planning. Nowadays, the application of artificial intelligence (AI) in radiation oncology has raised new hopes for generating high-quality dose distributions in a shorter timeframe, particularly due to the emergence of deep learning and its numerous applications in computer vision through convolutional neural networks (CNNs) [14–17]. CNN models facilitate the automated extraction of hierarchical features from image data, thus eliminating the need for image preprocessing, feature extraction, and dose calculations typically involved in multiple intermediate steps. The integrated complex network model directly outputs the complete 3D dose distribution map, thereby enabling end-to-end prediction. This automation eliminates laborious and error-prone manual operations, resulting in substantial time savings and enhanced accuracy in dose prediction during radiotherapy planning. Currently, prevailing approaches employ semantic segmentation models to perform various tasks using the same models. These models typically adopt an encoder-decoder structure, including U-Net and its variants [3, 18–20], and DeepLabV3 + [21]. Deep learning has been successfully applied to predict the dose distribution of radiotherapy for prostate cancer [20, 22], head and neck cancer [14, 23, 24], and lung cancer [19, 25], exhibiting promising outcomes.

Building on these advancements, researchers have posited that deep learning can be effectively applied to dose prediction for breast cancer, with several capable models already developed [26–29]. Currently, significant potential remains for further advancements in updating and enhancing the accuracy of models for breast cancer dose prediction. In this paper, we propose an end-to-end dose prediction model based on the 3D U-Net architecture for breast cancer radiotherapy, which assists planners in optimizing and refining the plan effectively.

2 Materials and methods

2.1 Patient database and data processing

As a retrospective study, a total of 176 breast cancer patients who received radiotherapy were selected for this study, none of them had undergone radiotherapy prior to this treatment. The dataset was randomly divided to form a training set of 141 patients, a validating set of 16 patients, and a testing set of 19 patients. The patients were treated in 25 fractions with a prescribed total dose of 50 Gy. The delivered volumetric modulated arc therapy (VMAT) plans were generated by experienced physicians using the Monaco treatment planning system. Additionally, this study has been approved by the ethics review board of Peking Union Medical College Hospital (PUMCH), China, with the approval ID being I-23PJ1938.

The patient's computed tomography (CT) data was acquired using the Brilliance CT Big Bore system (Philips Healthcare, Best, the Netherlands) with a slice thickness of 5 mm and a size of 512×512 pixels. The experienced radiation oncologists meticulously delineated the boundaries of the body, target regions, and OARs on the planning CT scan. The first clinical target volume (CTV1) represents the primary area of the left breast lesion, while CTV2 corresponds to the supraclavicular lymph node drainage region. To establish the planning target volume (PTV), comprising PTV1 and PTV2, the boundaries of CTV1 and CTV2 were extended by 0.5 cm in all three dimensions. And four OARs were included, the heart, lung L, lung R, and spinal cord. Additionally, to limit the scope of the image data, it was necessary to delineate the body's contour. However, the body mask was not input into the model during training. Each training sample input into the model contained one set of CT images, eight sets of outlined contours (two CTVs, two PTVs and four OARs), and one set of dose distribution images.

2.2 Model architecture and training

In this study, we first extended the standard 2D U-Net to 3D U-Net [30] and used this as a reference, benchmark and foundational network for dose prediction, followed by a series of optimization adjustments and improvements. Our model incorporated four key strategies, a double encoder combination attention (DECA) module, a cross stage partial + Resnet + Attention (CRA) module, a difficulty perception loss and a critical regions loss. The DECA module could extract features from two distinct data types and utilized 3D Channel Attention to integrate them, enabling the model to focus more accurately on the areas and features of OARs. The CRA module aided the model in more effectively extracting and concentrating on the data's useful features. The incorporation of a model-intrinsic difficulty perception loss assisted the model in identifying challenging areas, thereby enhancing learning in these regions. The purpose of a critical regions loss was to direct the model's attention more towards target volumes and critical OARs, while concurrently minimizing errors in these regions.

2.2.1 Network

The network in this paper featured a 5-layer structure, including two encoders and one decoder, as depicted in Fig. 1A. The input data size to the model was $n \times 9 \times 88 \times 512 \times 512$, where n represented the batch size. These input data were divided into two parts: the CT image with a size of $n \times 1 \times 88 \times 512 \times 512$, and the masks of PTVs and OARs with a size of $n \times 8 \times 88 \times 512 \times 512$. The entire model utilized Conv3D + InstanceNorm3d + ReLU as a convolution module. To address memory limitations, we employed a downsampling technique at the beginning of each encoder's processing, applying a $1 \times 7 \times 7$ convolution (stride = 2) and a $2 \times 2 \times 2$ MaxPool3d (stride = 2). The $1 \times 7 \times 7$ convolution also performed simple feature extraction while downsampling the data, thus preventing the loss of some details. Moreover, the final layer of the decoder included an output module where a $1 \times 1 \times 1$ convolution and the trilinear interpolation were upsampled to the input data size of $n \times 1 \times 88 \times 512 \times 512$. Additionally, to facilitate the computation of difficulty perception loss, an output module was integrated into each layer of the model. This configuration generated a complete output as well as four additional outputs during training, and only the complete output was utilized as the prediction result.

2.2.2 DECA module

To accurately emphasize regions and features of OARs, we introduced a DECA module to extract features from the CT and eight masks respectively, subsequently fusing them using 3D channel attention, as depicted in Fig. 1B. Due to the greater complexity and difficulty in extracting feature from CT images, the first encoder incorporated the CRA module, replacing the original two instances of 3D convolution. Conversely, the images from eight masks consisted solely of binary values (0 and 1), with voxels within the body assigned a value of 1, while the remaining voxels received a value of 0. These images required relatively simpler feature extraction, thus employing a standard dual-convolution module. For the dose prediction task, the CT data played a pivotal role by providing the necessary physical information, while the mask data facilitated the selection of specific tissues for training or validation. Through the DECA module, features could be extracted at various levels and scales.

2.2.3 CRA module

To enable the model to effectively extract and focus on relevant features of the data, the CRA module, comprising the cross stage partial (CSP) block [31], two Res blocks [32], and a 3D convolutional block attention module (CBAM) [33], was designed and is presented in Fig. 1C. This module utilized a transition layer composed solely of a $1 \times 1 \times 1$ convolution, serving as a hierarchical feature fusion mechanism designed to prevent duplicate gradient information across distinct layers. The model diagram illustrated the division of the module into two branches: the left branch functioned as a large residual path, wherein only the input content underwent a transition layer. Through the large residual path, the model directly learned high-level representations of the input feature map, thereby accelerating convergence speed and enhancing model accuracy. Conversely, the right branch was initiated by passing the input content through a transition layer, followed by two residual modules, a CBAM module, and another transition layer. The outputs from both branches were concatenated, and the features fused via the transition layer.

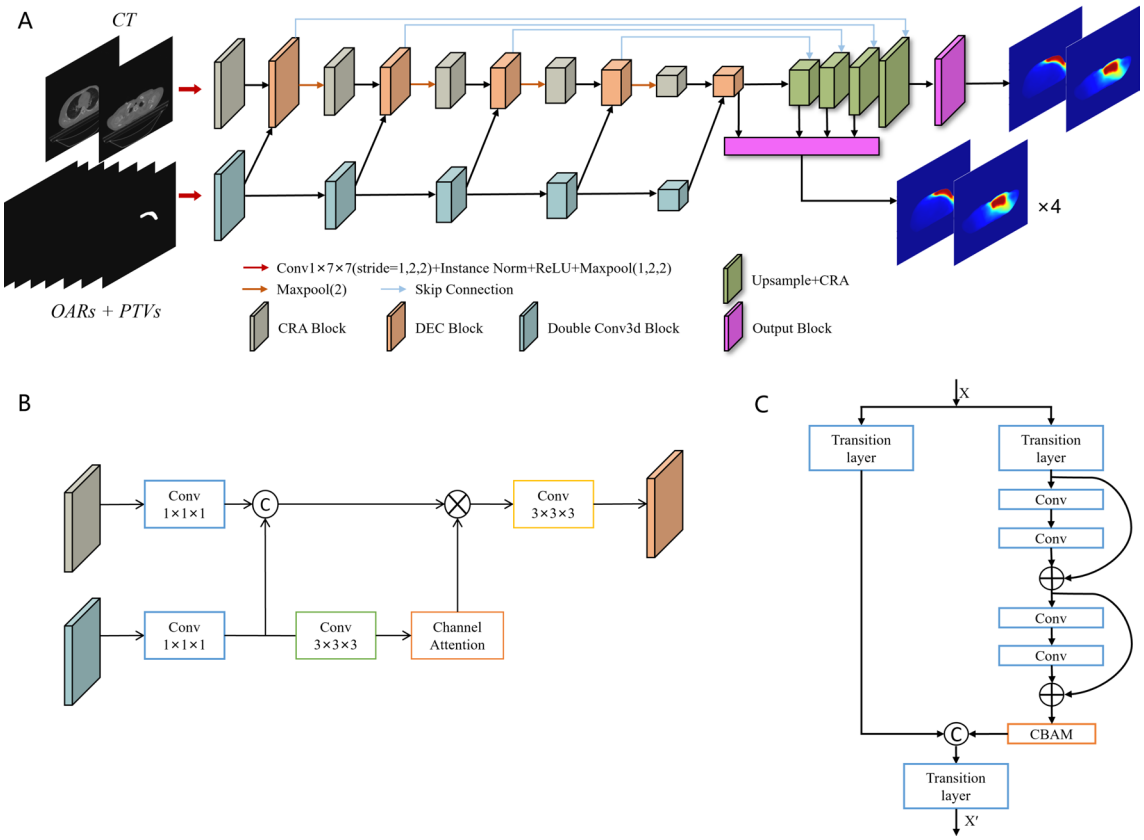

Fig. 1 The 3D architecture and proposed modules of the model in this paper. **A** the 3D architecture and network of the model. The network had a 5-layer structure, including two encoders and one decoder. The input data were divided into CT images and masks of PTVs and OARs. The whole model used Conv3D + InstanceNorm3d + ReLU as a convolution module. A complete output was generated as well as four additional outputs during training. **B** the DECA module. A DECA module was proposed to extract features from CT and 8 masks respectively, aiming to accurately emphasize regions and features of OARs. **C** the CRA module. The CRA module, based on the CSP Block, incorporated two Res blocks and a 3D CBAM attention module, and featured a Transition layer within the module. The CRA module facilitated the model's enhanced extraction and focused analysis of the data's useful features. CBAM: convolutional block attention module; CRA: CSP + Resnet + Attention; CSP: cross stage partial; CT: computed tomography; DECA: double encoder combination attention; OARs: organs at risk; PTV: planning target volume

2.2.4 Difficulty perception loss

The mean absolute error (MAE) is commonly used as a loss function in dose prediction process, as shown in Eq. (1). However, this average loss calculation tends to bias the model towards optimizing regions that are easier to predict, while struggling to optimize challenging regions [34]. Therefore, we need to put more attention to the challenging regions. To solve this problem, we proposed the difficulty perception loss to estimate and filter the difficult regions based on its own output. In this study, we used the mean squared error (MSE) loss to calculate the errors between the prediction results and the ground truth (GT), as demonstrated in Eq. (2):

$$L_{MAE} = \frac{1}{m}\sum_{n=1}^{m}\left|y_n - \hat{y_n}\right| \tag{1}$$

$$L_{MSE} = \frac{1}{m}\sum_{n=1}^{m}\left|y_n - \hat{y_n}\right|^2 \tag{2}$$

where $\hat{y_n}$ and y_n are respectively the dose prediction results and their corresponding ground truths, and m is the number of samples.

However, the central challenge lied in differentiating between difficult and easy areas. During a single forward propagation process, the model's output remained fixed, with some areas being learned effectively, while others were learned poorly.

Therefore, we proposed a difficulty perception function, which involved obtaining outputs from four different layers of the model, calculating the variance of these results to determine the dispersion across different areas, and utilizing this variance as the voxel score. This score was subsequently standardized to values between 0 and 1 using the perception function to generate a difficulty-aware map, representing the voxel-level weight. This voxel-level weight was then employed as the basis for the MSE loss calculation between the ground truth and prediction, with element-wise multiplication producing the final result.

$$f\left(s_1, s_2, s_3, s_4\right) = \frac{Var(S)}{\beta + Var(S)} \tag{3}$$

$$L_{DP} = \frac{1}{m} \sum_{n=1}^{m} \left| f_n\left(s_1, s_2, s_3, s_4\right) \bullet \left| y_n - \hat{y_n} \right|^2 \right| \tag{4}$$

As shown in the above equation, s_1, s_2, s_3, s_4 represent four output results and Var(S) is the variance of them, where β is the hyperparameter and $\beta > 0$ can adjust the normalized mapping to make it smoother and allow more attention to the difficult region. In this study, we made $\beta = 5$ and got expected results.

2.2.5 Critical regions loss

MAE loss and difficulty perception loss can significantly improve the overall results of dose prediction. To further reduce the maximum distribution error of the PTVs and OARs, we proposed the critical regions loss function, which focused only on the voxel area of PTVs and OARs. Since we believed that the PTVs and the OARs were equally important, we took their intersection and calculated the MSE result of this intersection.

$$L_{CR} = \frac{1}{m} \sum_{n=1}^{m} \left| y_n^r - \hat{y_n^r} \right|^2, \forall r \in V_P \cup V_O \tag{5}$$

where V_P and V_O represent the voxel area of PTVs and OARs, $\hat{y_n^r}$ and y_n^r are respectively the dose prediction results and their corresponding ground truths.

The final loss function used in this paper, combining the MAE loss, the difficulty perception loss and the critical regions loss, is:

$$L_{pred} = L_{MAE} + L_{DP} + L_{CR} \tag{6}$$

2.3 Prediction evaluation

To assess the performance and generalization capabilities of our model, we conducted an evaluation using a set of metrics [13, 18, 20, 27, 35] below.

a. Model performance metrics: The model's performance and generalization in dose prediction were assessed by the voxel MAE. The comparison of performance between different models was conducted by evaluating the magnitude of their respective MAE values.

b. Various dosimetric indexes of clinical interest: The effectiveness of our model was evaluated by several clinical assessment metrics, including the dose score, dose-volume histogram (DVH) score, conformity index (CI), and homogeneity index (HI) [36]. These dosimetric indexes could verify the consistency between the model's predictions and the actual treatment plans, a crucial factor for evaluating the model's practicality and establishing the foundation for its future refinement and clinical implementation. The calculations for CI and HI are presented in the following equations:

$$HI = \frac{D_2 - D_{98}}{D_{50}} \tag{7}$$

$$CI = \frac{V_{ref}}{V_{ptv}} \times \frac{V_{ref}}{V_{pres}} \tag{8}$$

where V_{ptv} and V_{pres} denote the volume of PTV and the prescription dose region, respectively, and V_{ref} denote the irradiated PTV volume of the prescription dose.

To assess the spatial dose distribution, more comprehensive metrics were chosen for PTVs and OARs, such as D_{mean} ,D_{max},D_{99},D_{98},D_{95},D_{50},D_{2},D_{1},$D_{0.1cc}$ for PTVs. D_x(Gy) is the prescription dose received for x% of the structure volume, D_{mean} is the mean dose of the structure, and D_{max} denote the maximum dose of the structure.

c. 3D gamma passing rates: The global 3D gamma analysis was used as a dose validation tool for the IMRT planning to further assess the accuracy of the voxel dose distribution prediction for OARs and PTVs, and was a common metric for dose validation [37], with the following equation:

$$\gamma\left(r_r, r_e\right) = \sqrt{\frac{r^2\left(r_r, r_e\right)}{\Delta d^2} + \frac{\delta^2\left(r_r, r_e\right)}{\Delta D^2}} \tag{9}$$

$$\delta^2\left(r_r, r_e\right) = \frac{\left[D\left(r_r\right) - D\left(r_e\right)\right]}{D_r^{max}} \times 100\% \tag{10}$$

$$\delta^2\left(r_r, r_e\right) = \frac{\left[D\left(r_r\right) - D\left(r_e\right)\right]}{D_r^{search\_max}} \times 100\% \tag{11}$$

And in this study, we set dose difference and distance-to-agreement criterion to be 3%/3 mm and 3%/2 mm, respectively, and the gamma passing rates were calculated above the threshold of 5% prescription dose.

d. Comparison with other models: To evaluate the performance of our model, we compared it with other models, including 3D U-Net, Cascade Unet3d [38] and HD Unet [39], as well as Unetr [40] and TransUnet [41], which employed the Transformer architecture. All models were trained on the same dataset, with the same loss function and the same batch size. The paired, two-tailed *t*-test was employed in comparison between our model and other models. And statistical analysis of the research data was performed using IBM SPSS 29.0. Statistical significance was established at p-value < 0.05 for all tests.

2.4 Experiment environment

All our experiments were conducted using PyTorch 1.10 and performed on an NVIDIA TITAN RTX GPU with 24 GB of memory. Our proposed method was trained using the Adam optimizer with a batch size of 1 for 300 epochs, and the model weights were initialized with the Kaiing initialization algorithm [42]. The initial learning rate was established at 0.0003, and a cosine annealing with restarts strategy was employed to progressively decrease it during training [43]. At the end of each training epoch, validation occurred on a validation set to assess the training status and ensure the effectiveness of the training. The model's loss reduction is depicted in Supplementary Fig. 3, demonstrating good training performance. Both training and validation losses followed a converging trend. The steep increases at the 20th, 40th, and 85th epochs were attributable to the use of the cosine annealing with restarts strategy, which prevented the loss function from falling into local minima and thus maintained a decreasing learning rate without improving model performance.

3 Results

3.1 3D dose distributions

Figure 2 shows four sets of longitudinal slices, denoted as A, B, C, and D. Slices A and B correspond to the two PTVs, while slices C and D pertain to relevant areas outside the PTVs. Each set of images, from left to right, shows the ground truth, 3D U-Net dose prediction results, the dose prediction results of our model, and the difference maps of voxel dose distributions between the two prediction results and the ground truth. Notably, as a visual comparison, Fig. 2 demonstrates that for both target-related and non-target-related regions, the predicted dose distribution closely resembles the ground truth, exhibiting smaller discrepancies in voxel doses compared to 3D U-Net and showcasing its accuracy and potential in dose distribution prediction.

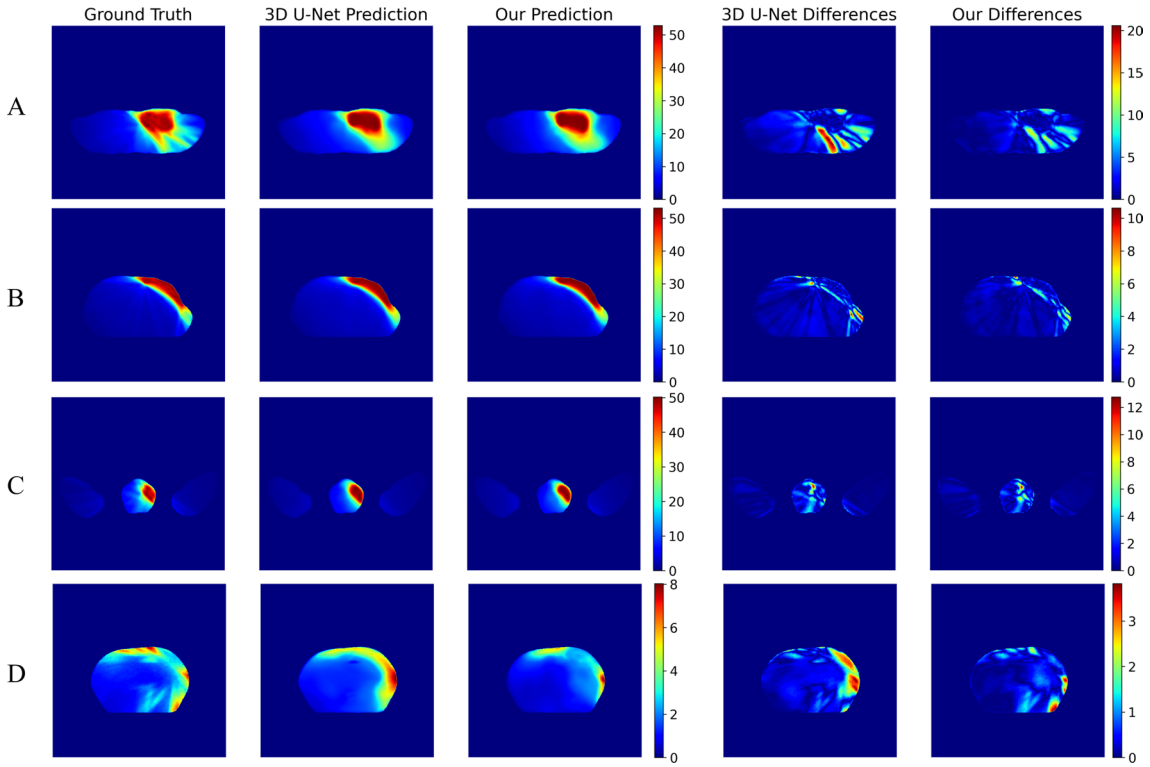

Fig. 2 Visual comparison of dose prediction results in one specific case. **A** and **B** two PTVs, **C** and **D** relevant areas outside the PTVs. Each set of images (from left to right): the ground truth, 3D U-Net dose prediction, our model's dose prediction, the difference map of 3D U-Net and the difference map of our model. The unit of color bar is Gy. PTV: planning target volume

3.2 Statistics of DVH dosimetric index

Figure 3 presents the comprehensive comparison of the DVHs for PTVs, CTVs and OARs in two randomly selected patients. The prescribed dose for them was 50 Gy. The figure clearly illustrates that the predictions for PTVs using our model exhibit a close fit to the ground truth curve, indicating its accuracy in dose distribution prediction. Additionally, although some OARs displayed notable differences in predicted doses, these variations were still within the clinically acceptable range.

The results of performance assessment for quantitatively relevant DVH indexes are shown as Table 1. The MAE and its standard deviation (Mean ± SD) between the ground truth and prediction results of both models were examined under

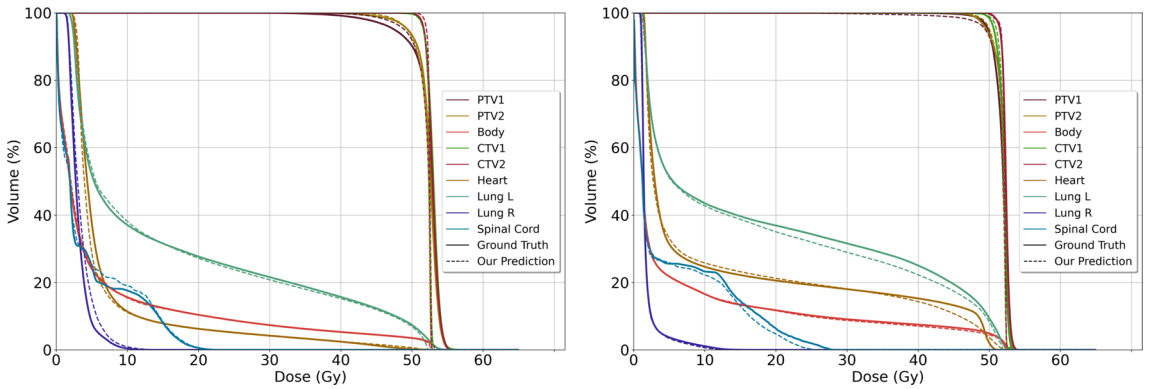

Fig. 3 The overall dose-volume histograms (DVHs) comparison of PTVs, CTVs and OARs between clinical (solid line) and predicted (dashed line) results in two randomly selected patients. The prescribed dose for them was 50 Gy. Lung L, left lung; Lung R, right lung; OARs: organs at risk; PTV: planning target volume

Table 1 Mean absolute errors (MAEs) and standard deviation (Mean ± SD) of dosimetric indexes for planned target volume (PTV)

	PTV1		PTV2	
	3D U-Net	Our	3D U-Net	Our
D_{98} (Gy)	5.07±4.64	3.30±3.62	2.82±3.44	0.97±1.52
D_{95} (Gy)	3.42±3.30	1.93±2.91	1.65±2.03	0.63±1.12
D_{50} (Gy)	0.41±0.37	0.37±0.38	0.36±0.29	0.27±0.22
D_2 (Gy)	0.86±0.47	1.14±0.41	1.08±0.50	1.13±0.37
D_{mean} (Gy)	0.89±0.61	0.62±0.58	0.53±0.52	0.28±0.22
HI	0.10±0.09	0.06±0.07	0.05±0.06	0.03±0.03
CI	0.05±0.05	0.04±0.04	0.03±0.02	0.02±0.01

A total dose of both PTV1 and PTV2 is 50 Gy

clinical criteria. It can be observed that our model exhibited a smaller discrepancy in dose predictions for PTVs, compared to 3D U-Net. And the MAEs of CI and HI were notably small, indicating that the algorithm presented in our study achieved enhanced consistency and homogeneity.

Figure 4 shows violin plots illustrating the data distribution and probability density of the mean and maximum dose differences. Both the mean and maximum dose difference of all OARs and CTVs primarily fell within the interquartile range. This indicated a favorable overall distribution of the results, with the median values closely approximating zero.

3.3 Comparison with other models

As shown in Table 2, to evaluate the performance of our model, we compared it with other models, including 3D U-Net, Cascade Unet3d [38] and HD Unet [39], as well as Unetr [40] and TransUnet [41], which employed the

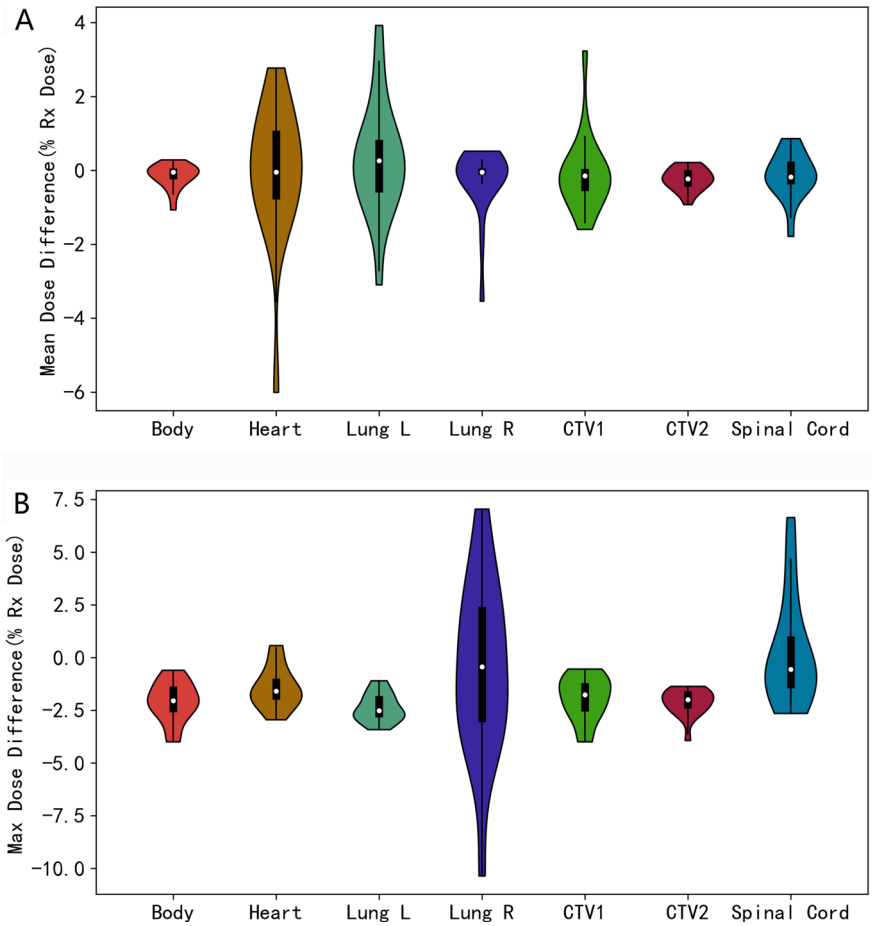

Fig. 4 Violin plots of the differences, normalized to the prescription dose, presenting **A** the mean dose difference and **B** the maximum dose difference in each OAR and CTV for all test patients. CTV: clinical target volume; OAR: organ at risk

Table 2 Comparison between our model and other excellent models

Methods	3D U-Net	Unetr [40]	TransUnet [41]	Cascade Unet3d [38]	HD Unet [39]	Our
Body (Gy)	1.29	1.34	1.21	1.23	1.38	**1.16**
p^{Body}	0.024*	0.016*	0.033*	0.191	0.001*	
PTV1 (Gy)	1.59	1.23	1.82	1.30	1.21	**1.03**
p^{PTV1}	< 0.001*	0.036*	< 0.001*	0.011*	0.007*	
PTV2 (Gy)	1.37	1.08	1.48	1.02	0.93	**0.74**
p^{PTV2}	< 0.001*	0.003*	< 0.001*	0.036*	0.022*	
CTV1 (Gy)	1.38	1.01	1.81	0.97	0.96	**0.90**
p^{CTV1}	< 0.001*	0.209	< 0.001*	0.120	0.254	
CTV2 (Gy)	1.09	0.74	1.43	0.71	0.67	**0.55**
p^{CTV2}	< 0.001*	0.011*	< 0.001*	0.091	0.028*	
Heart (Gy)	1.77	2.13	1.78	**1.62**	1.90	1.65
p^{Heart}	0.667	0.090	0.071	0.904	0.264	
Lung L (Gy)	1.91	2.12	1.83	1.77	2.22	**1.59**
p^{LL}	0.274	0.004*	0.046*	0.486	0.011*	
Lung R (Gy)	0.76	0.67	0.59	0.65	0.90	**0.57**
p^{LR}	0.035*	0.379	0.471	0.274	0.006*	
Spinal Cord (Gy)	0.78	0.95	0.77	0.88	0.90	**0.73**
p^{SC}	0.327	0.015*	0.651	0.028*	0.061	

*Statistically significant difference (paired, 2-tailed *t*-test, $p < 0.05$)

The mean absolute errors (MAEs) for Body, PTV, CTV, four OARs (Heart, Lung L, Lung R and Spinal Cord) are reported. p^x denotes the p-values obtained from pairwise comparisons between different models and our model across various regions (x = Body, PTV, CTV, four OARs)

Transformer architecture. The MAEs for each PTV, CTV and OAR are reported in Table 2, with Body representing the MAE in the effective area, thus indicating the overall model performance. In addition, it can be seen that our model demonstrated an error of less than 1.16 Gy in the total dose, meeting the clinical criteria. Furthermore, among the nine regions evaluated, eight regions achieved optimal levels of performance compared to other models. And the prediction errors for PTV1 and PTV2 were only 1.03 Gy and 0.74 Gy, respectively, with only a marginal deviation of 0.03 Gy from the optimal value, 1.62 Gy of Cascade Unet3d model, for the heart. Moreover, the critical OARs, the heart and lung L, achieved or approached optimal performance levels. And the majority of the model comparison results were statistically significant. For PTV1 and PTV2, comparisons between our model and other five models were all statistically significant. And Body and CTV2 exhibited statistically significance between our model and other four models, except Cascade Unet3d. Comparisons between our model and other three models, except 3D U-Net and Cascade Unet3d, were statistically significant for Lung L. For CTV1, Lung R and spinal cord, statistically significance existed only between our model and other two models. These results highlighted the exceptional overall performance of our model, establishing the groundwork for its subsequent clinical implementation.

Additionally, we conducted a comparative analysis of global 3D gamma, a critical tool for IMRT plan dose verification, to evaluate the accuracy of the predicted dose distribution across the four regions in the four models. Four regions included PTV1, PTV2, Heart and Lung L, while four models were 3D U-Net, Cascade Unet3d, HDUnet and our models, respectively. The gamma < 1 was tested, with the agreement assessed at a tolerance level of 3%/3 mm. The corresponding results are shown in Fig. 5 A. In our model, PTV1, PTV2, Heart, and Lung L exhibited mean gamma passing rates of 91.8%, 96.4%, 91.5%, and 93.2%, respectively. Importantly, all of these values surpassed the clinical criteria, superior to the other models. And the agreement, assessed at a tolerance level of 3%/2 mm, is shown in Fig. 5B. PTV1, PTV2, Heart, and Lung L exhibited mean gamma passing rates of 87.6%, 94.4%, 84.6%, and 86.8%. Besides, the blue plus sign in the figure shows some abnormal data, indicating that this model had less abnormal data and more focused results, proving its superior overall performance and prediction results.

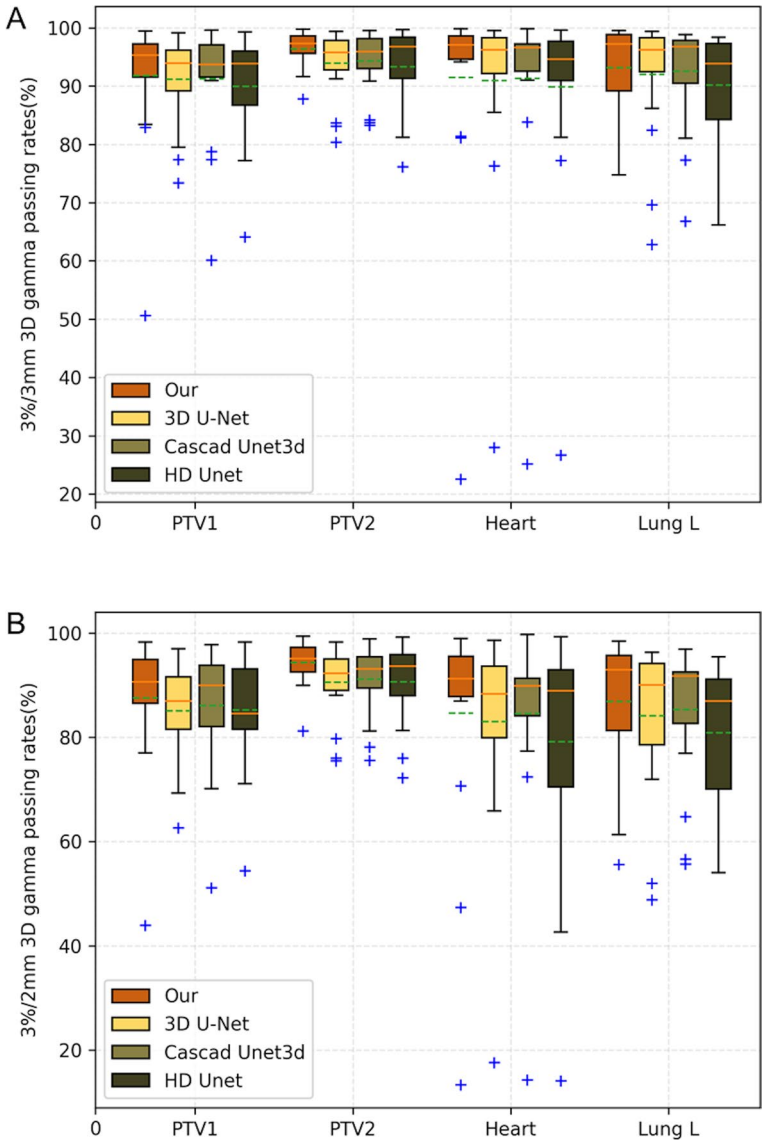

Fig. 5 Mean passing rates of 3D gamma analysis with 3% /3 mm and 3%/2 mm for four models in four areas. **A** 3D gamma passing rates accessed at a tolerance level of 3%/3 mm. **B** 3D gamma passing rates accessed at a tolerance level of 3%/2 mm. The solid orange line represents the median 3D gamma passing rates, and the dashed green line represents the mean 3D gamma passing rates

3.4 Model ablation experiments

To validate the effectiveness of each module proposed in the model, we conducted ablation experiments on the four key components. All methods were implemented under the same base model.

We present the detailed results in Table 3 to demonstrate the effectiveness of each module. As shown in Table 3, after incorporating the four key modules, the overall error of the model decreased by 0.07. Moreover, the errors for two target volumes, PTV1 and PTV2, decreased by 0.56 and 0.64, respectively. The errors for two critical OARs, Heart and Lung L, also decreased by 0.22 and 0.33, respectively. The difficulty perception module and DECA module exhibited the most significant effects. With the cumulative use of different modules, the error in most areas continued to decrease, although there were increases in some areas, such as Lung R and Spinal Cord, which increased by 0.02 and 0.07, respectively, after using the DECA module. However, this module also contributed to decreases of 0.1 in PTV1, 0.07 in PTV2, and 0.17 in Lung L. Thus, the increases in these two areas were within an acceptable range, particularly since these areas were not the primary focus, making the results acceptable.

Table 3 Validation of the different modules proposed in this study

DP	CRA	CR	DECA	Score	PTV1	PTV2	CTV1	CTV2	Heart	Lung L	Lung R	Spinal Cord
				1.23	1.59	1.37	1.38	1.09	1.77	1.91	0.76	0.78
√				1.20	1.29	0.83	1.32	0.93	1.65	1.72	0.62	0.69
√	√			1.18	1.16	0.85	1.04	0.65	1.60	1.81	0.59	0.71
√	√	√		1.16	1.13	0.80	1.06	0.62	1.58	1.75	0.55	0.66
√	√	√	√	**1.16**	**1.03**	**0.73**	**1.01**	**0.54**	**1.55**	**1.58**	0.57	0.73

CR: critical regions; CRA: cross stage partial + Resnet + Attention; DECA: double encoder combination attention; DP: difficulty perception

4 Discussion

As one of the most important methods to improve the quality and efficiency of radiotherapy planning, researchers have made significant efforts in dose prediction. The most widely used method, known as knowledge-based planning (KBP) [44–46], relies on a high-quality treatment planning database from previous patients. It utilizes patient-specific geometries to construct a dose correlation prediction model, estimating the optimal achievable DVH for new cases [47]. Additionally, this approach is currently available in commercial software such as RapidPlan developed by Varian [48]. Although KBP has demonstrated improvements in the quality and efficiency of treatment planning, it still exhibits several limitations such as a heavy reliance on small datasets, the need for manual feature design, the capacity to capture only low-level features, and the lack of spatial dose information in the contour structure [49–51]. Furthermore, the accuracy of predicting dose distributions remains limited [35, 47].

However, the application of deep learning and CNN models in radiation oncology has led to significant breakthroughs in dose learning. Kearney et al. [52] demonstrated that the 3D fully convolutional network, termed DoseNet, outperformed both the 2D fully convolutional and fully connected networks among the 3D U-Net-based models [53]. Liu et al. [54] proposed a network model called U-ResNet-D for accurate dose prediction in head and neck cancer. Moreover, Nguyen et al. [14] developed a fusion model combining U-Net and DenseNet for dose prediction in head and neck cancer patients, which surpassed the performance of both foundational models.

Although deep learning has been successfully applied to predict the dose distribution of many cancers, it still poses significant challenges for breast cancer. Firstly, it involves multiple target areas characterized by substantial variations and greater spatial distances due to respiratory motion, compared with other cancers, rendering the learning process more complex. In addition, breast cancer radiotherapy includes two critical OARs, the heart and lungs. Thus, to prevent surpassing clinical criteria and causing additional complications, it is imperative to significantly enhance the accuracy of dose prediction models.

In 2020, Bai et al. [55] employed three distinct atlas selection models to forecast 3D dose distributions in breast cancer patients, pioneering the use of 3D moment invariants (3DMI) for atlas image selection. This study presented a feasible dose distribution prediction framework based on deformable image registration (DIR), contributing to the improvement of treatment planning quality and efficiency. And Bakx et al. [27] proposed a deep learning model based on 2D U-net architecture to predict dose distributions for breast cancer in 2021, compared with a commercially available contextual atlas regression forest (cARF) model. The results indicated that both models could produce clinically acceptable plans. Hedden et al. [13] developed two deep learning models, one 2D and the other 3D, both based on the U-net architecture, utilizing a training set of 120 patients and a testing set of 25 patients. These models were capable of predicting dose distributions utilizing anatomical information and dose prescriptions. The study results indicated that both models were able to generate clinically acceptable dose distributions, with the 3D model performing better than the 2D model. In 2021, Ahn et al. [26] also employed deep learning to develop a patient-specific dose prediction model for left-sided breast clinical cases and compared its performance with traditional KBP using RapidPlan. The study utilized a database of 50 VMAT plans involving left-sided breast cancer patients to generate training and validation datasets, and the results demonstrated that the dose predictions from deep learning were superior to those generated by VMAT plans from RapidPlan. However, these studies have certain limitations. Some of the datasets they utilized were restricted in number of patients, and there was a lack of in-depth exploration in terms of updates to the deep learning models and the accuracy of dose prediction.

In this study, we proposed an end-to-end dose prediction model based on a 3D U-Net architecture. This model successfully and accurately predicted dose distributions for various patients with left-sided breast cancer. The predicted dose distributions closely resembled the ground truth at each dose level, and overall dose differences were smaller compared to the baseline 3D U-Net model, making predictions more precise. We also conducted a comparative analysis between our model and several current models, the quantitative results showed that our model outperformed other models.

However, the model may still need further improvement. While the addition of diverse modules to the 3D U-Net model allowed enhanced feature coverage and improved prediction accuracy, the error in some regions increased with the cumulative utilization of different modules. Although our model exhibited an increase in error solely within a few unfocused regions such as Lung R and Spinal Cord, all of which were within acceptable ranges, there still remained potential for further investigation to identify an optimal combination of module additions that can yield even better results. Additionally, this model has not yet undergone evaluation for its effectiveness and efficiency in dose prediction within actual clinical settings. Future work will involve conducting prospective studies to further explore and validate this model's potential to enhance radiotherapy planning quality and efficiency in clinical settings, thereby demonstrating its benefits.

Dose distribution prediction serves as a valuable quality control tool in clinical treatment planning. Physicists can use dose prediction to assess whether the current plan is adequate or where improvements can be made, and physicians can use it to promptly adjust the dose constraint requirements for OARs, significantly reducing the time required for plan design. Furthermore, the adoption of dose distribution prediction establishes a novel quality standard for treatment plans, enhancing consistency and high quality of treatment plans through the prediction models. These objectives have motivated researchers to explore the application of AI in dose distribution prediction, consequently fostering the rapid development of dose prediction models.

For breast cancer radiotherapy, advancements in technologies such as Deep Inspiration Breath Holding (DIBH) [56–58] have introduced multiple radiotherapy methods, necessitating the selection of the optimal method for individual patients. Our model can address this challenge by predicting the dose distribution in advance based on the patient's imaging characteristics. This approach not only saves considerable time and labor costs but also enhances the efficiency of selecting the most suitable radiotherapy method for each patient, ultimately leading to improved treatment outcomes and minimized radiation doses to OARs. As a result, our model exhibits significant potential for further exploration across diverse applications.

5 Conclusions

In this study, we developed an end-to-end dose prediction model for breast cancer radiotherapy, using a DECA module, and added a CRA module to improve the model's feature extraction capability for CT data. The results show that the model can perform more accurate dose predictions compared to other advanced models. Accurate dose prediction can greatly improve the quality and efficiency of treatment planning, explore the possibility of automatic plan implementation, and help different breast cancer patients select more suitable radiotherapy methods and develop personalized treatment plans.

Author contributions All authors contributed to the study conception and design. Zhikai Liu and Xiaorong Hou made substantial contributions to the conception and design of the work. Material preparation, data collection and analysis were performed by Weishi Cheng, Yimeng Zhang, Jing Shen and Hui Guan. The creation of new software used in the work was performed by Yimeng Zhang, Lu Bai and Shaobin Wang. The first draft of the manuscript was written by Weishi Cheng and Xiaorong Hou, and all authors commented on previous versions of the manuscript. All authors read and approved the final manuscript.

Funding The work that was described in this paper was supported by a grant from National High Level Hospital Clinical Research Funding (Grant Number 2022-PUMCH-A-104). We would like to extend our gratitude to the funder.

Data availability The datasets analysed during the study are not publicly available due to the privacy of patient information but are available from the corresponding author on reasonable request.

Code availability This work is not applicable for this section.

Declarations

Ethics approval and consent to participate This study was performed in line with the principles of the Declaration of Helsinki. Approval was granted by the Ethics Committee of Peking Union Medical College Hospital (PUMCH), China, with the approval ID being I-23PJ1938. Informed consent was obtained from all individual participants and/or their legal guardians included in this study.

Competing interests The authors declare no competing interests.

References

1. Otto K. Volumetric modulated arc therapy: IMRT in a single gantry arc. Med Phys. 2008;35:310–7.
2. Quan EM, Li X, Li Y, Wang X, Kudchadker RJ, Johnson JL, et al. A comprehensive comparison of IMRT and VMAT plan quality for prostate cancer treatment. Int J Radiat Oncol Biol Phys. 2012;83:1169–78. https://doi.org/10.1016/j.ijrobp.2011.09.015.
3. Osman AFI, Tamam NM. Attention-aware 3D U-Net convolutional neural network for knowledge-based planning 3D dose distribution prediction of head-and-neck cancer. J Appl Clin Med Phys. 2022;23: e13630. https://doi.org/10.1002/acm2.13630.
4. Wang C, Zhu X, Hong JC, Zheng D. Artificial Intelligence in radiotherapy treatment planning: present and future. Technol Cancer Res Treat. 2019;18:1533033819873922. https://doi.org/10.1177/1533033819873922.
5. Nguyen D, Long T, Jia X, Lu W, Gu X, Iqbal Z, et al. A feasibility study for predicting optimal radiation therapy dose distributions of prostate cancer patients from patient anatomy using deep learning. Sci Rep. 2019;9:1076. https://doi.org/10.1038/s41598-018-37741-x.
6. Nelms BE, Robinson G, Markham J, Velasco K, Boyd S, Narayan S, et al. Variation in external beam treatment plan quality: an inter-institutional study of planners and planning systems. Pract Radiat Oncol. 2012;2:296–305. https://doi.org/10.1016/j.prro.2011.11.012.
7. Batumalai V, Jameson MG, Forstner DF, Vial P, Holloway LC. How important is dosimetrist experience for intensity modulated radiation therapy? A comparative analysis of a head and neck case. Pract Radiat Oncol. 2013. https://doi.org/10.1016/j.prro.2012.06.009.
8. Jensen AR, Nellemann HM, Overgaard J. Tumor progression in waiting time for radiotherapy in head and neck cancer. Radiother Oncol. 2007. https://doi.org/10.1016/j.radonc.2007.04.001.
9. Marcello M, Ebert M, Haworth A, Steigler A, Kennedy A, Joseph D, et al. Association between treatment planning and delivery factors and disease progression in prostate cancer radiotherapy: results from the TROG 03.04 RADAR trial. Radiother Oncol. 2018;126:249–56. https://doi.org/10.1016/j.radonc.2017.10.021.
10. Hébert-Croteau N, Freeman CR, Latreille J, Rivard M, Brisson J. A population-based study of the impact of delaying radiotherapy after conservative surgery for breast cancer. Breast Cancer Res Treat. 2004;88:187–96.
11. Gupta S, King WD, Korzeniowski M, Wallace DL, Mackillop WJ. The effect of waiting times for postoperative radiotherapy on outcomes for women receiving partial mastectomy for breast cancer: a systematic review and meta-analysis. Clin Oncol. 2016;28:739–49. https://doi.org/10.1016/j.clon.2016.07.010.
12. Benk V, Joseph L, Fortin P, Zhang G, Belisle P, Levinton C, et al. Effect of delay in initiating radiotherapy for patients with early stage breast cancer. Clin Oncol (R Coll Radiol). 2004. https://doi.org/10.1016/j.clon.2003.10.008.
13. Hedden N, Xu H. Radiation therapy dose prediction for left-sided breast cancers using two-dimensional and three-dimensional deep learning models. Phys Med. 2021;83:101–7. https://doi.org/10.1016/j.ejmp.2021.02.021.
14. Nguyen D, Jia X, Sher D, Lin M-H, Iqbal Z, Liu H, et al. 3D radiotherapy dose prediction on head and neck cancer patients with a hierarchically densely connected U-net deep learning architecture. Phys Med Biol. 2019;64: 065020. https://doi.org/10.1088/1361-6560/ab039b.
15. Mahmood R, Babier A, McNiven A, Diamant A, Chan TCY. Automated Treatment Planning in Radiation Therapy using Generative Adversarial Networks. In: Finale D-V, Jim F, Ken J, David K, Rajesh R, Byron W, et al., editors. Proceedings of the 3rd Machine Learning for Healthcare Conference; Proceedings of Machine Learning Research: PMLR; 2018. 484--99.
16. Babier A, Mahmood R, McNiven AL, Diamant A, Chan TCY. Knowledge-based automated planning with three-dimensional generative adversarial networks. Med Phys. 2020;47:297–306. https://doi.org/10.1002/mp.13896.
17. Nguyen D, McBeth R, Sadeghnejad Barkousaraie A, Bohara G, Shen C, Jia X, et al. Incorporating human and learned domain knowledge into training deep neural networks: a differentiable dose-volume histogram and adversarial inspired framework for generating Pareto optimal dose distributions in radiation therapy. Med Phys. 2020;47:837–49. https://doi.org/10.1002/mp.13955.
18. Cros S, Bouttier H, Nguyen-Tan PF, Vorontsov E, Kadoury S. Combining dense elements with attention mechanisms for 3D radiotherapy dose prediction on head and neck cancers. J Appl Clin Med Phys. 2022;23: e13655. https://doi.org/10.1002/acm2.13655.
19. Jhanwar G, Dahiya N, Ghahremani P, Zarepisheh M, Nadeem S. Domain knowledge driven 3D dose prediction using moment-based loss function. Phys Med Biol. 2022. https://doi.org/10.1088/1361-6560/ac8d45.
20. Ma J, Nguyen D, Bai T, Folkerts M, Jia X, Lu W, et al. A feasibility study on deep learning-based individualized 3D dose distribution prediction. Med Phys. 2021;48:4438–47. https://doi.org/10.1002/mp.15025.

21. Han EY, Cardenas CE, Nguyen C, Hancock D, Xiao Y, Mumme R, et al. Clinical implementation of automated treatment planning for whole-brain radiotherapy. J Appl Clin Med Phys. 2021. https://doi.org/10.1002/acm2.13350.
22. Kontaxis C, Bol GH, Lagendijk JJW, Raaymakers BW. DeepDose: towards a fast dose calculation engine for radiation therapy using deep learning. Phys Med Biol. 2020;65: 075013. https://doi.org/10.1088/1361-6560/ab7630.
23. Gronberg MP, Gay SS, Netherton TJ, Rhee DJ, Court LE, Cardenas CE. Technical note: dose prediction for head and neck radiotherapy using a three-dimensional dense dilated U-net architecture. Med Phys. 2021;48:5567–73. https://doi.org/10.1002/mp.14827.
24. Fan J, Wang J, Chen Z, Hu C, Zhang Z, Hu W. Automatic treatment planning based on three-dimensional dose distribution predicted from deep learning technique. Med Phys. 2019;46:370–81. https://doi.org/10.1002/mp.13271.
25. Xing Y, Zhang Y, Nguyen D, Lin M-H, Lu W, Jiang S. Boosting radiotherapy dose calculation accuracy with deep learning. J Appl Clin Med Phys. 2020;21:149–59. https://doi.org/10.1002/acm2.12937.
26. Ahn SH, Kim E, Kim C, Cheon W, Kim M, Lee SB, et al. Deep learning method for prediction of patient-specific dose distribution in breast cancer. Radiat Oncol. 2021;16:154. https://doi.org/10.1186/s13014-021-01864-9.
27. Bakx N, Bluemink H, Hagelaar E, van der Sangen M, Theuws J, Hurkmans C. Development and evaluation of radiotherapy deep learning dose prediction models for breast cancer. Phys Imaging Radiat Oncol. 2021;17:65–70. https://doi.org/10.1016/j.phro.2021.01.006.
28. Kneepkens E, Bakx N, van der Sangen M, Theuws J, van der Toorn P-P, Rijkaart D, et al. Clinical evaluation of two AI models for automated breast cancer plan generation. Radiat Oncol. 2022;17:25. https://doi.org/10.1186/s13014-022-01993-9.
29. Ravari ME, Nasseri S, Mohammadi M, Behmadi M, Ghiasi-Shirazi SK, Momennezhad M. Deep-learning method for the prediction of three-dimensional dose distribution for left breast cancer conformal radiation therapy. Clin Oncol (R Coll Radiol). 2023;35:e666–75. https://doi.org/10.1016/j.clon.2023.09.002.
30. Çiçek Ö, Abdulkadir A, Lienkamp SS, Brox T, Ronneberger O. 3D U-Net learning dense volumetric segmentation from sparse annotation. Medical image computing and computer-assisted intervention—MICCAI 2016. Cham: Springer International Publishing; 2016.
31. Wang CY, Liao HYM, Wu YH, Chen PY, Hsieh JW, Yeh IH, CSPNet: A New Backbone that can Enhance Learning Capability of CNN. 2020 IEEE/CVF Conference on Computer Vision and Pattern Recognition Workshops (CVPRW); 2020; 14–19
32. He K, Zhang X, Ren S, Sun J, editors. Deep Residual Learning for Image Recognition. 2016 IEEE Conference on Computer Vision and Pattern Recognition (CVPR); 2016; 27–30.
33. Woo S, Park J, Lee J-Y, Kweon I-S. CBAM: convolutional block attention module. In: Ferrari V, Hebert M, Sminchisescu C, Weiss Y, editors. European conference on computer vision. Cham: Springer International Publishing; 2018.
34. Huber PJ. Robust estimation of a location parameter. In: Johnson NL, Kotz S, editors. Breakthroughs in Statistics Methodology and Distribution. New York: Springer New York; 1992. p. 492–518.
35. Bohara G, Sadeghnejad Barkousaraie A, Jiang S, Nguyen D. Using deep learning to predict beam-tunable Pareto optimal dose distribution for intensity-modulated radiation therapy. Med Phys. 2020;47:3898–912. https://doi.org/10.1002/mp.14374.
36. Babier A, Zhang B, Mahmood R, Moore KL, Purdie TG, McNiven AL, et al. OpenKBP: The open-access knowledge-based planning grand challenge and dataset. Med Phys. 2021;48:5549–61. https://doi.org/10.1002/mp.14845.
37. Low DA, Harms WB, Mutic S, Purdy JA. A technique for the quantitative evaluation of dose distributions. Med Phys. 1998;25:656–61.
38. Isensee F, Jaeger PF, Kohl SAA, Petersen J, Maier-Hein KH. nnU-Net: a self-configuring method for deep learning-based biomedical image segmentation. Nat Methods. 2021;18:203–11. https://doi.org/10.1038/s41592-020-01008-z.
39. Çiçek Ö, Abdulkadir A, Lienkamp SS, Brox T, Ronneberger O. 3D U-Net: learning dense volumetric segmentation from sparse annotation. In: Ourselin S, Joskowicz L, Sabuncu MR, Unal G, Wells W, editors. International conference on medical image computing and computer-assisted intervention. Cham: Springer International Publishing; 2016.
40. Hatamizadeh A, Yang D, Roth HR, Xu D. UNETR: transformers for 3D medical image segmentation. IEEE/CVF Winter Conf Appl Comput Vision. 2022;2021:1748–58.
41. Chen J, Lu Y, Yu Q, Luo X, Adeli E, Wang Y, et al. TransUNet: transformers make strong encoders for medical image segmentation. arXiv. 2021. https://doi.org/10.48550/arXiv.2102.04306.
42. He K, Zhang X, Ren S, Sun J, editors. Delving deep into rectifiers: surpassing human-level performance on imagenet classification. 2015 IEEE International Conference on Computer Vision (ICCV); 2015;7–13.
43. Loshchilov I, Hutter F. Sgdr: stochastic gradient descent with warm restarts. arXiv. 2016. https://doi.org/10.48550/arXiv.1608.03983.
44. Wilkins DE, Des JM. A call for knowledge-based planning. AI Mag. 2001;22:99. https://doi.org/10.1609/aimag.v22i1.1547.
45. Zhang J, Wu QJ, Xie T, Sheng Y, Yin F-F, Ge Y. An ensemble approach to knowledge-based intensity-modulated radiation therapy planning. Front Oncol. 2018. https://doi.org/10.3389/fonc.2018.00057.
46. Ge Y, Wu QJ. Knowledge-based planning for intensity-modulated radiation therapy: a review of data-driven approaches. Med Phys. 2019;46:2760–75. https://doi.org/10.1002/mp.13526.
47. Zhou J, Peng Z, Song Y, Chang Y, Pei X, Sheng L, et al. A method of using deep learning to predict three-dimensional dose distributions for intensity-modulated radiotherapy of rectal cancer. J Appl Clin Med Phys. 2020;21:26–37. https://doi.org/10.1002/acm2.12849.
48. Systems VM. DVH estimation models for rapid plan. In: Eclipse photon and electron instruction for use. Varian Medical Systems: Palo Alto; 2014. p. 183–204.
49. Tol JP, Delaney AR, Dahele M, Slotman BJ, Verbakel WFAR. Evaluation of a knowledge-based planning solution for head and neck cancer. Int J Radiat Oncol Biol Phys. 2015;91:612–20. https://doi.org/10.1016/j.ijrobp.2014.11.014.
50. Yang Y, Ford EC, Wu B, Pinkawa M, van Triest B, Campbell P, et al. An overlap-volume-histogram based method for rectal dose prediction and automated treatment planning in the external beam prostate radiotherapy following hydrogel injection. Med Phys. 2013;40: 011709. https://doi.org/10.1118/1.4769424.
51. Wang Y, Heijmen BJM, Petit SF. Prospective clinical validation of independent DVH prediction for plan QA in automatic treatment planning for prostate cancer patients. Radiother Oncol. 2017;125:500–6. https://doi.org/10.1016/j.radonc.2017.09.021.
52. Kearney V, Chan JW, Haaf S, Descovich M, Solberg TD. DoseNet: a volumetric dose prediction algorithm using 3D fully-convolutional neural networks. Phys Med Biol. 2018;63: 235022. https://doi.org/10.1088/1361-6560/aaef74.
53. Shiraishi S, Moore KL. Knowledge-based prediction of three-dimensional dose distributions for external beam radiotherapy. Med Phys. 2016;43:378. https://doi.org/10.1118/1.4938583.

54. Liu Z, Fan J, Li M, Yan H, Hu Z, Huang P, et al. A deep learning method for prediction of three-dimensional dose distribution of helical tomotherapy. Med Phys. 2019;46:1972–83. https://doi.org/10.1002/mp.13490.
55. Bai X, Wang B, Wang S, Wu Z, Gou C, Hou Q. Radiotherapy dose distribution prediction for breast cancer using deformable image registration. Biomed Eng Online. 2020;19:39. https://doi.org/10.1186/s12938-020-00783-2.
56. Vander Veken L, Van Ooteghem G, Razavi A, Da Rita QS, Longton E, Kirkove C, et al. Voluntary versus mechanically-induced deep inspiration breath-hold for left breast cancer: a randomized controlled trial. Radiother Oncol. 2023;183: 109598. https://doi.org/10.1016/j.radonc.2023.109598.
57. Parsons D, Joo M, Iqbal Z, Godley A, Kim N, Spangler A, et al. Stability and reproducibility comparisons between deep inspiration breath-hold techniques for left-sided breast cancer patients: a prospective study. J Appl Clin Med Phys. 2023;24: e13906. https://doi.org/10.1002/acm2.13906.
58. Wolf J, Stoller S, Lübke J, Rothe T, Serpa M, Scholber J, et al. Deep inspiration breath-hold radiation therapy in left-sided breast cancer patients: a single-institution retrospective dosimetric analysis of organs at risk doses. Strahlenther Onkol. 2023;199:379–88. https://doi.org/10.1007/s00066-022-01998-z.